Coupled-Wave Theory for Square-Lattice Photonic Crystal Lasers With TE Polarization

Kyosuke Sakai, *Member, IEEE*, Eiji Miyai, and Susumu Noda, *Fellow, IEEE*

***Abstract*—We present a coupled-wave analysis for square-lattice photonic crystal lasers with transverse electric polarization. A model consisting of eight plane waves coupled by Bragg diffraction is used to describe two-dimensional optical coupling. The resonant frequencies and threshold criteria for the modes of oscillation have been determined for the case of index periodicity with a lattice of circular holes. The spatial intensity distributions of these resonant modes have also been calculated. For the fundamental modes, we have investigated how the intensity distribution varies as a function of coupling strength. The dependence of the threshold gain of these modes on hole size has also been elucidated. This semianalytical approach provides a comprehensive understanding of square-lattice photonic crystal lasers and allows more effective optimization of their cavity design.**

***Index Terms*—Coupled mode analysis, distributed feedback devices, laser cavity resonators, surface-emitting lasers.**

I. Introduction

TWO-DIMENSIONAL (2-D) photonic crystal (PC) lasers have attracted much attention due to their capability of large-area coherent oscillation based on the band edge effect [1]–[7]. Single longitudinal and transverse mode oscillation in two dimensions can essentially be achieved even with a large lasing area, which allows high-power, single-mode operation. The output power is coupled to the vertical direction by the PC itself; these systems thus operate as surface-emitting lasers. The surface-emitted beam resulting from a large lasing area has a small beam divergence angle [8] and, moreover, both the polarization and beam pattern can be controlled by appropriate design of the PC unit cell and/or lattice phase [3], [7]. The lasing wavelength of 2-D PC lasers has recently been extended from the visible and near infrared regime to the mid-infrared [9], terahertz [10], [11], and blue-violet regime [12], [13].

Manuscript received September 01, 2009; revised November 09, 2009. Current version published March 03, 2010. This work was supported by JSPS Research Fellowships for Young Scientists, and partly supported by Special Coordination Funds for Promoting Science and Technology (SCF) commissioned by the Ministry of Education, Culture, Sports, Science and Technology (MEXT) of Japan, and Core Research for Evolutional Science and Technology–Japan Science and Technology Agency (CREST-JST).

K. Sakai is with Pioneering Research Unit for Next Generation, Kyoto University, Kyoto 615-8245, Japan (e-mail: sakai@qoe.kuee.kyoto-u.ac.jp).

E. Miyai was with Kyoto University, Kyoto, 615-8150, Japan. He is now with Photonics Research and Development Center, ROHM, Kyoto 615-8585, Japan (e-mail: eiji.miyai@dsn.rohm.co.jp).

S. Noda is with the Department of Electric Science and Engineering, and also with the Photonics and Electronics Science and Engineering Center, Kyoto University, Kyoto 615-8510, Japan (e-mail: snoda@kuee.kyoto-u.ac.jp).

Digital Object Identifier 10.1109/JQE.2009.2037597

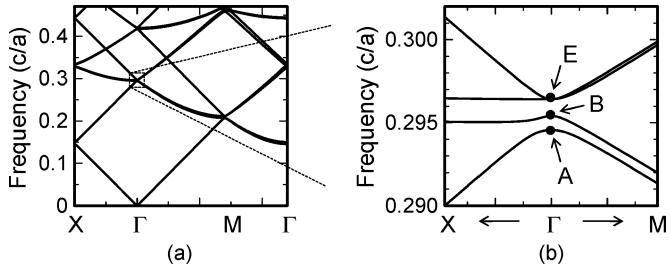

Fig. 1. (a) Band structure for square lattice photonic crystal with TE polarization. (b) Magnified band structure in the vicinity of the Γ-point, which is the point of interest in this paper.

Until now, theoretical analyses of PC lasers have been carried out using the plane-wave expansion method (PWEM) [4], the finite-difference time-domain (FDTD) method [14] and the time-domain Fourier–Galerkin (TDFG) method [6]. Fig. 1(a) shows a typical photonic band structure for a square-lattice crystal with transverse electric (TE) polarization, and Fig. 1(b) shows the detailed band structure around the Γ-point where surface emission is obtained. Resonant mode oscillations are formed at the edges of the band structure, indicated by the three dots, and the lasing oscillation occurs at the mode with the lowest threshold gain, i.e., the smallest loss [15]. Therefore, it is essential to evaluate the threshold gain of the resonant modes at the band edges in order to arrive at a comprehensive understanding of the device characteristics. Analysis of the threshold criteria for the different modes of oscillation is difficult using the theoretical methods mentioned above, because the PWEM is only valid for infinite structures and the FDTD method requires enormous computer resources to model the finite structures of actual devices. An analysis based on the TDFG method concluded that the square lattice with TE polarization is not a viable choice for the realization of large-area coherent emission, which contradicts the experimental results of [3], [7], and [8]. In contrast, calculations based on a coupled-wave model [16] enable compact analysis of the resonant mode threshold for finite-structure PC lasers. We have recently performed coupled-wave analysis for a square lattice structure with transverse magnetic (TM) polarization [17]. However, no analysis for TE polarization has yet been reported. In this paper, we develop the coupled-wave analysis method to include square lattice structures with TE polarization and give the threshold criteria for the modes of oscillation. Our analysis employs the eight-wave model [18], which is able to describe the coupling of two light waves propagating in orthogonal directions, giving rise to large-area 2-D coherent oscillation.

We derive coupled-wave equations and coupling constants for a square lattice of circular holes in Section II. In Section III, the

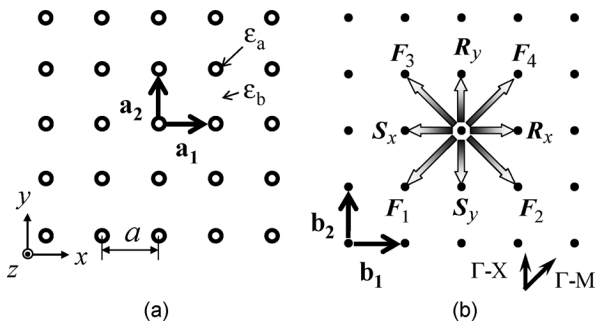

Fig. 2. (a) Schematic illustration of a square lattice photonic crystal. (b) Corresponding reciprocal lattice showing the wave vectors considered in this paper.

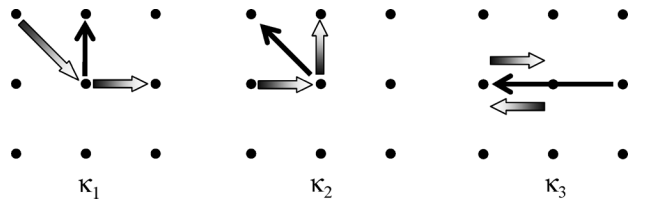

Fig. 3. Diffraction diagram for each coupling constant. Shaded arrows indicate pairs of wave vectors and black arrows indicate the corresponding reciprocal lattice vectors.

resonant mode frequencies, threshold gains and envelope profile of the intensity distribution in the finite-size photonic crystal cavity are numerically calculated. The threshold gains of the fundamental modes are also investigated as a function of hole size. A summary of the results is given in Section IV.

II. Coupled-Wave Model

The PC structure investigated here consists of a square lattice of circular holes in the x–y plane with period a, as shown in Fig. 2(a). The dielectric constants of the circular holes and the background material are $\varepsilon_{\rm a}$ and $\varepsilon_{\rm b}$, respectively. The structure is assumed to be uniform in the z-direction. The circular holes form a 2-D Bravais lattice with sites given by the vectors:

$$\mathbf{X}(l) = l_1\mathbf{a}_1 + l_2\mathbf{a}_2. \tag{1}$$

Here, $\mathbf{a}_1$ and $\mathbf{a}_2$ are the two primitive translation vectors of the lattice, while l_1 and l_2 are any two integers. The area enclosed by the primitive unit cell of this lattice is $a_{\rm c} = |\mathbf{a}_1 \times \mathbf{a}_2| = a^2$.

The corresponding reciprocal lattice is shown in Fig. 2(b); the reciprocal lattice vectors $\mathbf{G}(h)$ are given by

$$\mathbf{G}(h) = h_1\mathbf{b}_1 + h_2\mathbf{b}_2. \tag{2}$$

Here, h_1 and h_2 are any two integers, denoted collectively by h, and the primitive translation vectors of this lattice are given by

$$\mathbf{b}_1 = \frac{2\pi}{a_c}\left(a_y^{(2)}, -a_x^{(2)}\right) \tag{3}$$

$$\mathbf{b}_2 = \frac{2\pi}{a_c}\left(-a_y^{(1)}, a_x^{(1)}\right) \tag{4}$$

where $a_j^{(i)}$ is the $j^{\rm th}$ Cartesian component, x or y, of $\mathbf{a}_i$ ($i = 1$ or 2). If we express the primitive translation vectors as $\mathbf{a}_1 = (a, 0)$ and $\mathbf{a}_2 = (0, a)$, as shown in Fig. 2(a), the primitive reciprocal lattice vectors are $\mathbf{b}_1 = (2\pi/a, 0)$ and $\mathbf{b}_2 = (0, 2\pi/a)$, as shown in Fig. 2(b). The shaded arrows indicate the wave vectors of the plane waves that have significant intensity at the band edges shown in Fig. 1(b). For the analysis of other band edges, we would first need to find the specific wave vectors that have significant contributions at those points.

The scalar wave equations for the magnetic field H_z for TE polarization are written in the form [19]

$$\frac{\partial}{\partial x}\left\{\frac{1}{k^2}\frac{\partial H_z}{\partial x}\right\} + \frac{\partial}{\partial y}\left\{\frac{1}{k^2}\frac{\partial H_z}{\partial y}\right\} + H_z = 0. \tag{5}$$

Here, the constant k is given by [20]

$$k^2 = \left(\frac{2\pi}{\lambda}\right)^2 \sum_{\mathbf{G}} \varepsilon_{\mathbf{G}} e^{i\mathbf{G}\cdot\mathbf{r}} + i\frac{2\pi\varepsilon_0^{1/2}}{\lambda}\sum_{\mathbf{G}} \alpha_{\mathbf{G}} e^{i\mathbf{G}\cdot\mathbf{r}}. \tag{6}$$

We note that the sign of the second term was negative in [20]. In the above expression, λ is the wavelength of light in free space, $\varepsilon_{\mathbf{G}}$ is the Fourier coefficient of the modulated dielectric constant $\varepsilon(\mathbf{r})$, $\varepsilon_0 (= \varepsilon_{\mathbf{G}=0})$ is the averaged dielectric constant, and $\alpha_{\mathbf{G}}$ is the Fourier coefficient of the modulated gain constant $\alpha(\mathbf{r})$. It is assumed that the gain is small over distances of the order of a wavelength and that the modulations of the dielectric constant and gain constant are small, such that

$$\begin{aligned} \alpha &\ll \beta \equiv \frac{2\pi\varepsilon_0^{1/2}}{\lambda} \\ \alpha_{\mathbf{G}} &\ll \beta \\ \varepsilon_{\mathbf{G}\neq 0} &\ll \varepsilon_0. \end{aligned} \tag{7}$$

These assumptions allow us to express the constant k in the form

$$\frac{1}{k^2} = \frac{1}{\beta^4}\left(\beta^2 - i2\alpha\beta + 2\beta\sum_{\mathbf{G}\neq 0}\kappa_{\mathbf{G}} e^{i\mathbf{G}\cdot\mathbf{r}}\right). \tag{8}$$

Here, $\alpha (= \alpha_{\mathbf{G}=\mathbf{0}}/2)$ is the averaged gain constant and $\kappa_{\mathbf{G}}$ is the coupling constant defined as

$$\kappa_{\mathbf{G}} = -\frac{\pi}{\lambda\varepsilon_0^{1/2}}\varepsilon_{\mathbf{G}} - i\frac{\alpha_{\mathbf{G}}}{2}. \tag{9}$$

In the present analysis, we consider the resonance at the Γ-point shown in Fig. 1(b), in which the coupling constants for $|\mathbf{G}| = 2\pi/a$, $2\sqrt{2}\pi/a$ and $4\pi/a$ contribute significantly. We list the corresponding coupling constants as follows:

$$\kappa_1 = \kappa_{\mathbf{G}}\big|_{|\mathbf{G}|=\beta_0} \tag{10}$$

$$\kappa_2 = \kappa_{\mathbf{G}}\big|_{|\mathbf{G}|=\sqrt{2}\beta_0} \tag{11}$$

$$\kappa_3 = \kappa_{\mathbf{G}}\big|_{|\mathbf{G}|=2\beta_0} \tag{12}$$

where $\beta_0 = 2\pi/a$. Fig. 3 shows a schematic illustration of the pairs of wave vectors that are coupled in each of these three cases. Coupling constant κ_1 describes the intensity of the coupling of two plane waves propagating at 45° to each other, whereas κ_2 describes the intensity of the coupling of plane waves propagating in directions perpendicular to each other.

Coupling constant κ_3 describes the intensity of the coupling of counterpropagating waves, which corresponds to the backward scattering in second-order distributed feedback (DFB) lasers. In the case of a square lattice with TE polarization, the coupling constant κ_2 does not exist. This is because the electric

fields of two waves propagating in perpendicular directions are orthogonal to each other and the overlap integral vanishes. The 2-D coupling is therefore described by the coupling constant κ_1.

In a periodic structure, the magnetic field is given by the Bloch mode [19]

$$H_z(\mathbf{r}) = \sum_{\mathbf{G}} H_{\mathbf{G}} \exp\left[-i(\mathbf{k}+\mathbf{G})\cdot\mathbf{r}\right] \tag{13}$$

where $H_{\mathbf{G}}$ is the amplitude of each plane wave, and $\mathbf{k}$ is a wave vector in the first Brillouin zone that becomes zero at the Γ-point. In principle, a periodic perturbation of the medium generates an infinite set of diffraction orders. However, at the specific Γ-point discussed in this paper, the amplitudes $H_{\mathbf{G}}$ with $|\mathbf{G}| = \beta_0$ are significant and plane waves with $|\mathbf{G}| = \sqrt{2}\beta_0$ play a significant role in 2-D coupling [18]. Therefore, eight waves with $|\mathbf{G}| = \beta_0$ and $|\mathbf{G}| = \sqrt{2}\beta_0$ are considered in our model, indicated by the shaded arrows in Fig. 2(b). Using these eight waves, we rewrite the expression for the magnetic field as the following sum:

$$\begin{aligned} H_z(\mathbf{r}) = {} & R_x e^{-i\beta_0 x} + S_x e^{i\beta_0 x} + R_y e^{-i\beta_0 y} + S_y e^{i\beta_0 y} \\ & + F_1 e^{i\beta_0 x + i\beta_0 y} + F_2 e^{-i\beta_0 x + i\beta_0 y} + F_3 e^{i\beta_0 x - i\beta_0 y} \\ & + F_4 e^{-i\beta_0 x - i\beta_0 y} \end{aligned} \tag{14}$$

where R_x, S_x, R_y, and S_y are the complex amplitudes of the waves propagating along the x or y ($\Gamma - \mathrm{X}$) directions, whereas F_i ($i = 1$ to 4) are the complex amplitudes of the waves propagating along the Γ–M directions, as illustrated in Fig. 2(b). These eight waves propagating in the PC structure interfere with each other due to diffraction by the circular holes. As a result, the amplitudes of the waves are position dependent and we can express these amplitudes as a function of position; this model is thus able to treat the finite structures. In order to simplify the equations, we write the amplitudes as R_x instead of $R_x(\mathbf{r})$. In view of (7), these amplitudes vary slowly enough that their second derivatives can be neglected. By substituting (8) and (14) into (5), then using (10) and (12) and comparing the exponential terms, we obtain eight equations of the form:

$$\begin{aligned} & -\frac{\partial}{\partial x}R_x + (\alpha - i\delta)R_x \\ & \quad = i\kappa_3 S_x - i\kappa_1 F_2 - i\kappa_1 F_4 \end{aligned} \tag{15a}$$

$$\begin{aligned} & \frac{\partial}{\partial x}S_x + (\alpha - i\delta)S_x \\ & \quad = i\kappa_3 R_x - i\kappa_1 F_1 - i\kappa_1 F_3 \end{aligned} \tag{15b}$$

$$\begin{aligned} & -\frac{\partial}{\partial y}R_y + (\alpha - i\delta)R_y \\ & \quad = i\kappa_3 S_y - i\kappa_1 F_3 - i\kappa_1 F_4 \end{aligned} \tag{15c}$$

$$\begin{aligned} & \frac{\partial}{\partial y}S_y + (\alpha - i\delta)S_y \\ & \quad = i\kappa_3 R_y - i\kappa_1 F_1 - i\kappa_1 F_2 \end{aligned} \tag{15d}$$

$$\begin{aligned} & \frac{\partial}{\partial x}F_1 + \frac{\partial}{\partial y}F_1 + (2\alpha - i\delta)F_1 + i\frac{\beta_0}{2}F_1 \\ & \quad = -i\kappa_1 S_x - i\kappa_1 S_y \end{aligned} \tag{15e}$$

$$\begin{aligned} & -\frac{\partial}{\partial x}F_2 + \frac{\partial}{\partial y}F_2 + (2\alpha - i\delta)F_2 + i\frac{\beta_0}{2}F_2 \\ & \quad = -i\kappa_1 R_x - i\kappa_1 S_y \end{aligned} \tag{15f}$$

$$\begin{aligned} & \frac{\partial}{\partial x}F_3 - \frac{\partial}{\partial y}F_3 + (2\alpha - i\delta)F_3 + i\frac{\beta_0}{2}F_3 \\ & \quad = -i\kappa_1 S_x - i\kappa_1 R_y \end{aligned} \tag{15g}$$

$$\begin{aligned} & -\frac{\partial}{\partial x}F_4 - \frac{\partial}{\partial y}F_4 + (2\alpha - i\delta)F_4 + i\frac{\beta_0}{2}F_4 \\ & \quad = -i\kappa_1 R_x - i\kappa_1 R_y. \end{aligned} \tag{15h}$$

The parameter δ is a normalized frequency defined by

$$\delta \equiv \frac{\beta^2 - \beta_0^2}{2\beta_0} \approx \beta - \beta_0 = n(\omega - \omega_0)/c \tag{16}$$

where n is the averaged refractive index, which is equal to $\varepsilon_0^{1/2}$ and c is the speed of light in free space. The parameter δ is a measure of the deviation of the oscillation frequency ω from the Bragg frequency ω_0. The Bragg frequency corresponds to the wavelength of light within the PC structure ($\lambda/\varepsilon_0^{1/2}$) that equals the period a. Because this frequency deviation is assumed to be small, we have set $\beta/\beta_0 \approx 1$ in the above derivation.

The above set of equations expresses the coupling of waves propagating in the square-lattice PC structure. For example, (15a) describes the coupling of waves R_x and S_x that travel in opposite directions; the intensity is given by coupling constant κ_3. The same equation also describes the coupling of waves that propagate in oblique directions. That is, wave R_x propagating along the x-axis couples to waves F_2 and F_4 with the coupling constant κ_1. Equations (15f) and (15h) describe the coupling of wave F_2 to wave S_y and wave F_4 to wave R_y, respectively, both with an intensity given by coupling constant κ_1. Waves S_y and R_y propagate along the y-axis. Therefore, these oblique couplings with constant κ_1 provide 2-D optical feedback, which gives rise to coherent 2-D oscillation. We note that coupling constant κ_2, which describes the intensity of the direct coupling of waves propagating perpendicular to each other along the x and y axes, does not exist in the set of (15), as also pointed out in [18]. On the left-hand side of (15e)–(15h), we can neglect both the first two derivatives and the third terms in each case, because the amplitudes vary only slowly and α and δ are much smaller than β_0 for the lower-order resonant modes. Subsequently, by substituting (15e)–(15h) into (15a)–(15d) and including diffraction in the direction vertical to the PC plane represented by the coupling constant κ_0 [6], [22],[1] we obtain four equations of the form

$$\begin{aligned} (\alpha - \kappa_0 - i\delta)R_x - \frac{\partial}{\partial x}R_x = {} & i\frac{4\kappa_1^2}{\beta_0}R_x + (i\kappa_3 - \kappa_0)S_x \\ & + i\frac{2\kappa_1^2}{\beta_0}S_y + i\frac{2\kappa_1^2}{\beta_0}R_y \end{aligned} \tag{17a}$$

$$\begin{aligned} (\alpha - \kappa_0 - i\delta)S_x + \frac{\partial}{\partial x}S_x = {} & i\frac{4\kappa_1^2}{\beta_0}S_x + (i\kappa_3 - \kappa_0)R_x \\ & + i\frac{2\kappa_1^2}{\beta_0}S_y + i\frac{2\kappa_1^2}{\beta_0}R_y \end{aligned} \tag{17b}$$

$$\begin{aligned} (\alpha - \kappa_0 - i\delta)R_y - \frac{\partial}{\partial y}R_y = {} & i\frac{4\kappa_1^2}{\beta_0}R_y + (i\kappa_3 - \kappa_0)S_y \\ & + i\frac{2\kappa_1^2}{\beta_0}S_x + i\frac{2\kappa_1^2}{\beta_0}R_x \end{aligned} \tag{17c}$$

[1] κ_0 corresponds to h_1 in this reference.

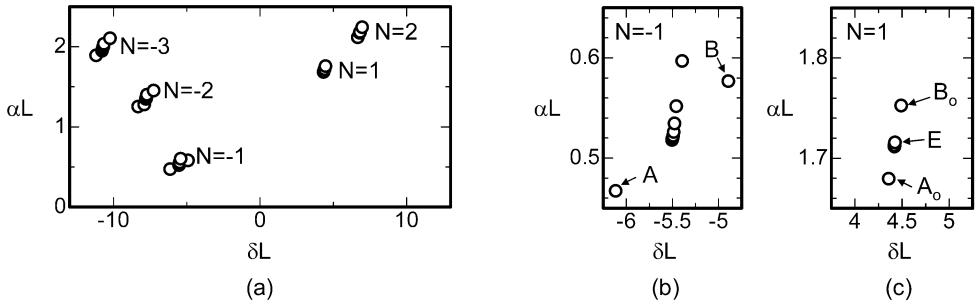

Fig. 4. (a) Gain required for threshold as a function of frequency deviation from the Bragg condition. (b) Magnified plot for modes $\mathrm{N} = -1$, and (c) for $\mathrm{N} = 1$.

$$(\alpha - \kappa_0 - i\delta)S_y + \frac{\partial}{\partial y}S_y = i\frac{4\kappa_1^2}{\beta_0}S_y + (i\kappa_3 - \kappa_0)R_y + i\frac{2\kappa_1^2}{\beta_0}S_x + i\frac{2\kappa_1^2}{\beta_0}R_x. \quad (17d)$$

By numerically solving this set of (17) under some boundary conditions, the eigenvalues α and δ provide the threshold gain and the frequency deviation from the Bragg condition, respectively, for the resonant mode in a square-lattice PC cavity with TE polarization. We note that for other crystal geometries such as triangular-lattice PCs, a different set of equations, as shown in [21], is required.

The coupling constants for the circular holes are given in the form

$$\kappa_{\mathbf{G}} = \left\{-\frac{\pi}{a\varepsilon_0}(\varepsilon_\mathrm{a} - \varepsilon_\mathrm{b}) - i\frac{1}{2}(\alpha_\mathrm{a} - \alpha_\mathrm{b})\right\}\frac{2fJ_1(|\mathbf{G}|R)}{(|\mathbf{G}|R)}. \quad (18)$$

Here, ε_a and ε_b are the dielectric constants and α_a and α_b are the gain constants of the circular holes and the background material, respectively. The quantity f is a hole-filling factor given by $f = \pi R^2/a^2$, R is the radius of the circular hole, and $J_1(x)$ is a Bessel function of the first kind for integer order one. The averaged dielectric constant ε_0 is given by $\varepsilon_0 = \sqrt{\varepsilon_\mathrm{a} f + \varepsilon_\mathrm{b}(1-f)}$. We exclusively define the vertical coupling constant κ_0 using the relation $\kappa_0 \mathrm{L} = 2\kappa_1^2 \mathrm{L}^2/500$,[2] where L is the length of the PC cavity.

In this work, we assume a square PC region with a side of length L, and apply the boundary conditions of zero reflectivity and zero gain perturbation $(\alpha_\mathrm{a} - \alpha_\mathrm{b})$. In order to solve the set of (17), we multiplied these equations by length L and used the finite difference method as described in the Appendix. The magnetic field distribution H_z can be obtained by substituting the resultant complex amplitudes of the waves into (13), whereas the electric field distribution $\mathbf{E}(\mathbf{r},t) = (E_x \exp(i\omega t), E_y \exp(i\omega t), 0)$ is calculated using the time-dependent magnetic field $\mathbf{H}(\mathbf{r},t) = (0, 0, H_z \exp(i\omega t))$ and Maxwell's equation

$$\nabla \times \mathbf{H}(\mathbf{r},t) = \varepsilon(\mathbf{r})\frac{\partial \mathbf{E}(\mathbf{r},t)}{\partial t}. \quad (19)$$

The intensity envelope (mode pattern) of the resonant mode throughout the PC structure is determined using the sum $R_x R_x^* + S_x S_x^* + R_y R_y^* + S_y S_y^*$.

[2]This relation was determined empirically. Details will be discussed elsewhere.

III. Numerical Results

In this section, we describe the results of numerical calculations based on the coupled wave equations (17). We have obtained data for the frequency, threshold gain and intensity pattern of the resonant modes in the square PC cavity. The PC structure was defined by the following parameters: the dielectric constants $\varepsilon_a = 9.8$ and $\varepsilon_b = 12.0$, the gain perturbation $(\alpha_\mathrm{a} - \alpha_\mathrm{b}) = 0$ (index coupling), the hole-filling factor $f = 0.18$, the lattice period $a = 290$ nm, and the PC cavity length $L = 50\,\mu$m. The corresponding input parameters for (17) are $\kappa_0 \mathrm{L} = 0.71$, $\kappa_1 \mathrm{L} = 13.29$, $\kappa_3 \mathrm{L} = 4.0$, and $\beta_0 \mathrm{L} = 1100$. These input parameters express the feedback strength of the PC cavity, which should greatly affect the mode patterns and the threshold gain. Thus, we have also calculated the mode patterns for several different coupling strengths and have evaluated the threshold gain as a function of the hole-filling factor.

A. Mode Spectra

Fig. 4(a) shows the threshold gain $(\alpha\mathrm{L})$ and the frequency deviation $(\delta\mathrm{L})$ from the Bragg condition for the resonant modes. The threshold gain increases for larger frequency deviations.

We classify the groups of resonances as $\mathrm{N} = \pm 1, \pm 2, \pm 3, \ldots$ according to their frequency deviation from the Bragg condition, where N is the mode number in [16]. Modes with a larger absolute value of N consist of a higher order longitudinal mode (i.e., a standing wave formed by R_x and S_x possesses a higher order profile along the x direction). Fig. 4(b) and (c) shows more detailed plots for modes $\mathrm{N} = 1$ and $\mathrm{N} = -1$, respectively. Modes A, B, and E are fundamental modes that have a single-lobed intensity pattern throughout the photonic crystal. These fundamental modes correspond to the resonant modes at the band edge in Fig. 1(b). Mode A has the lowest frequency of these three modes, and mode E is doubly degenerate. Modes A and B have twin modes $\mathrm{A_o}$ and $\mathrm{B_o}$, respectively, which have zero intensity at the center of the structure. The other points in Fig. 4(b) and (c) correspond to higher order modes that are all doubly degenerate. These higher order modes consist of a higher order transverse mode (i.e., a standing wave formed by R_x and S_x possesses a higher order profile along the y direction). We note that there are many higher order modes in the vicinity of mode E, but they are hardly distinguishable in Fig. 4(c). The threshold gain of modes A, B, and E are $\alpha_\mathrm{A}\mathrm{L} = 0.467$, $\alpha_\mathrm{B}\mathrm{L} = 0.576$, and $\alpha_\mathrm{E}\mathrm{L} = 1.715$, respectively. Because it has the lowest threshold gain, lasing oscillation is expected to occur at mode A.

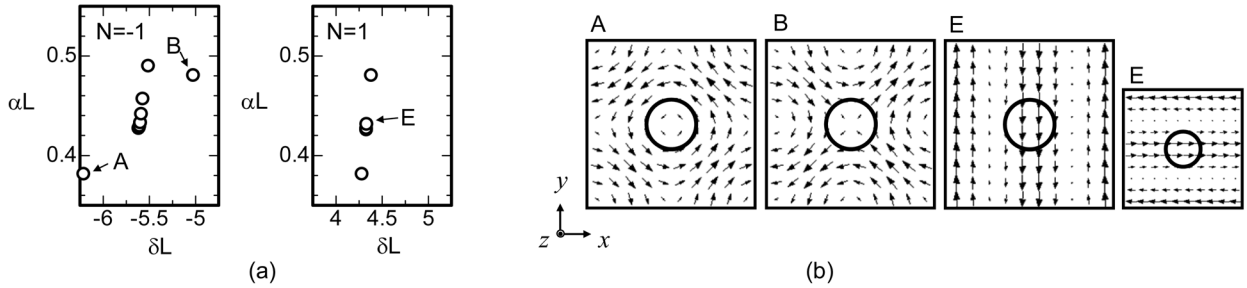

Fig. 5. (a) Threshold gain as a function of frequency deviation with $\kappa_0 = 0$. (b) Electric field distributions around the air hole for the fundamental modes A, B, and E.

Experimentally, we have previously observed lasing oscillation at the lowest frequency band edge, which corresponds to mode A [15].

The threshold gain of each resonant mode originates in the emission loss from the photonic crystal cavity, i.e., both emission from the edges of the square crystal region and surface emission. To elucidate the origin of the threshold difference among the fundamental modes, we first calculated the threshold gain for zero surface emission (we set $\kappa_0 = 0$). In this case, the threshold gain of mode E greatly decreased and became comparable to that of modes A and B ($\alpha_{\mathrm{A}}\mathrm{L} = 0.38$, $\alpha_{\mathrm{B}}\mathrm{L} = 0.48$, $\alpha_{\mathrm{E}}\mathrm{L} = 0.43$), as shown in Fig. 5(a). Thus, the major source of loss for mode E is surface emission. The degree of surface emission is strongly dependent on the symmetric nature of the electric field with respect to the center of the lattice hole [23]. Fig. 5(b) shows the electric field distribution of each fundamental resonant mode around the hole. Modes A and B are antisymmetric in nature, which leads to destructive interference in the direction vertical to the crystal plane and thus reduces the surface emission. In contrast, modes E are symmetric and hence the resulting constructive interference gives rise to a larger degree of surface emission. The difference in threshold gain between modes A and B in Fig. 5(a) indicates that the emission loss from the edges of the cavity differs. In order to understand the origin of this difference, we performed calculations with $\kappa_1 = 0$ and $\kappa_0 = 0$, where both the 2-D coupling and the surface emission vanish. In this case, modes A and B become degenerate ($\delta_{\mathrm{A}}\mathrm{L} = \delta_{\mathrm{B}}\mathrm{L} = -4.97$, $\delta_{\mathrm{E}}\mathrm{L} = 4.97$) and all the fundamental modes possess the same threshold gain ($\alpha_{\mathrm{A}}\mathrm{L} = \alpha_{\mathrm{B}}\mathrm{L} = \alpha_{\mathrm{E}}\mathrm{L} = 0.43$). This result indicates that the 2-D coupling induces the splitting between modes A and B. Therefore, with stronger 2-D coupling we can expect a higher mode selectivity, i.e., a larger difference in threshold gain of modes A and B. The splitting in frequency between mode A (or B) and mode E is induced by backward coupling (κ_3). This splitting corresponds to the stopband in 1-D DFB lasers, which is induced by coupling between the counterpropagating waves.

B. Mode Pattern

The eigenvectors of (17) provide the complex amplitudes R_x, S_x, R_y, and S_y, which are functions of the positions x and y. The intensity envelope (mode pattern) of the resonant mode throughout the PC structure can be determined from these amplitudes using the sum $R_x R_x^* + S_x S_x^* + R_y R_y^* + S_y S_y^*$. Fig. 6 illustrates the intensity envelopes of the fundamental modes (A, B, and E). Modes A and B show single-peak profiles, whereas the doubly degenerate mode E shows a saddle-shaped pattern. In contrast, modes $\mathrm{A_o}$ and $\mathrm{B_o}$ exhibit vase-like patterns with zero intensity at the center of the structure, as shown in Fig. 7(a). Fig. 7(b) illustrates the intensity envelope for the higher order modes around mode E, which have several nodes and antinodes. The envelopes of other higher order modes also exhibit a series of nodes and antinodes.

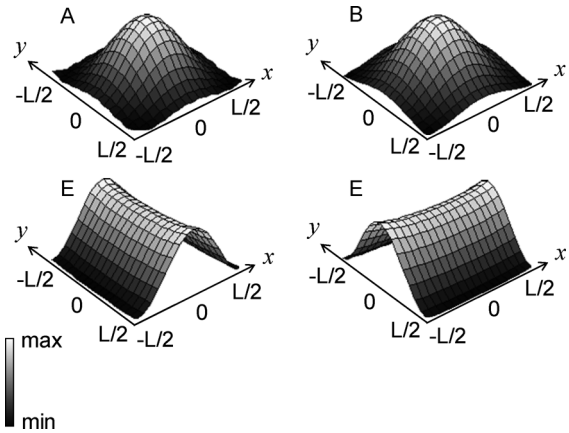

Fig. 6. Spatial intensity distributions for the fundamental modes.

Fig. 8 illustrates the cross-sectional intensity distribution along the x-axis ($y = 0$) for mode A with various values of coupling strength $\kappa_3\mathrm{L}$; the difference in dielectric constants, $\varepsilon_a - \varepsilon_b$, is changed while maintaining the same hole-filling factor of $f = 0.18$ and lattice period of $a = 290$ nm. The other two coupling constants $\kappa_0\mathrm{L}$ and $\kappa_1\mathrm{L}$ are calculated accordingly. We distinguish three different types of patterns that depend on the coupling strength, analogous to the situation for a 1-D DFB laser [16]. When the coupling is small, for example $\kappa_0\mathrm{L} = 0.01$, $\kappa_1\mathrm{L} = 1.66$, and $\kappa_3\mathrm{L} = 0.5$, the intensity pattern decreases in the middle region of the structure and peaks at the ends. In contrast, when the coupling is large, for example $\kappa_0\mathrm{L} = 0.71$, $\kappa_1\mathrm{L} = 13.29$, and $\kappa_3\mathrm{L} = 4.0$, the intensity pattern peaks at the center of the structure and decays towards the ends. These two types of behavior are balanced for a coupling strength of $\kappa_3\mathrm{L} = 1.5$ ($\kappa_0\mathrm{L} = 0.10$, $\kappa_1\mathrm{L} = 4.99$), where the intensity is more or less uniformly distributed throughout the whole PC structure. These types of behavior also apply to the other fundamental modes B and E.

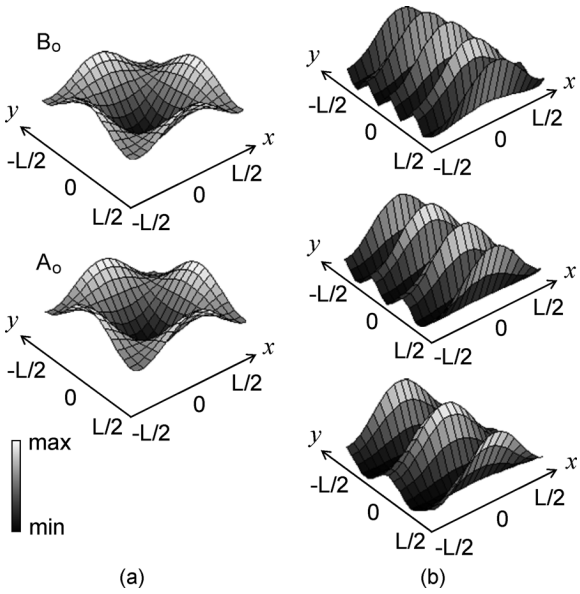

Fig. 7. Spatial intensity distributions for (a) mode A_0 and mode B_0, and for (b) higher order modes adjacent to mode E.

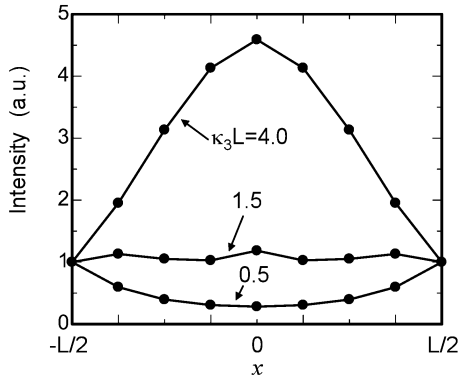

Fig. 8. Cross-sectional intensity distributions ($y = 0$) along the x-axis for mode A.

C. Threshold Gain as a Function of Hole Filling Factor

The analyses above were carried out for a constant hole filling factor of $f = 0.18$. However, the coupling constants are a function of f and hence the threshold gain should also be strongly dependent on f. Fig. 9(a) shows the coupling constants as a function of the hole filling factor. We note that κ_3 becomes zero at approximately $f = 0.3$, which implies that the backward diffraction vanishes. Fig. 9(b) shows the threshold gain of the fundamental modes A, B, and E as a function of hole filling factor. The threshold gain for modes A and B drastically increases in the region of $f = 0.3$, at which point (17) diverge. This occurs because the degree of backward diffraction becomes very small and there is insufficient optical confinement. This result indicates that the coupling constant κ_3 is the dominant factor determining the degree of optical confinement in the current system, a square lattice with TE polarization. We note that in a square lattice with TM polarization, even if the backward diffraction vanishes in the vicinity of $f = 0.3$, sufficient optical confinement is obtained due to the 2-D coupling constant κ_2

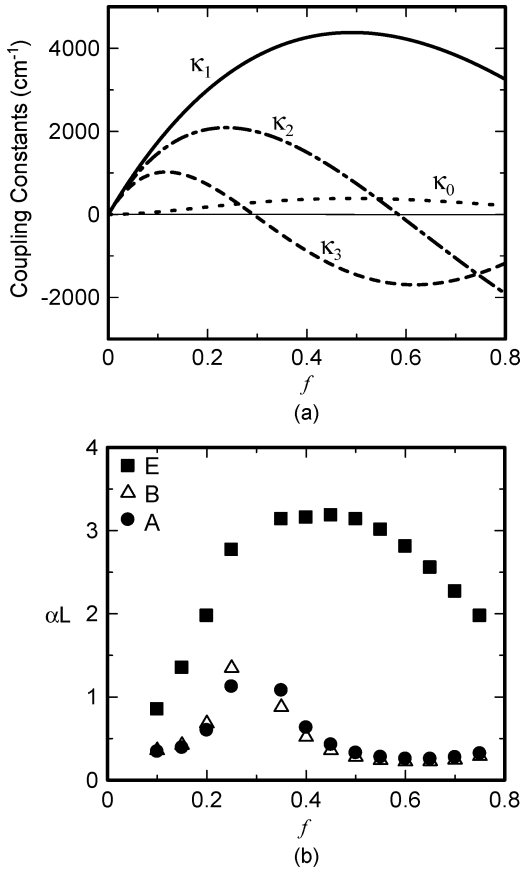

Fig. 9. (a) Coupling constants as a function of hole filling factor. (b) Gain required for threshold as a function of hole filling factor for the fundamental modes A, B, and E.

[17]. Fig. 9(b) indicates that the lowest threshold gain switches from mode A to mode B when the hole filling factor passes $f = 0.3$. This allows mode selection between modes A and B by controlling the hole-filling factor.

IV. Conclusion

We have presented a coupled-wave analysis for square-lattice photonic crystal lasers with transverse electric polarization. We have numerically calculated the resonant frequencies, threshold conditions and the intensity patterns of the modes of oscillation for the case of index periodicity with a lattice of circular holes. We have demonstrated that the fundamental modes, which correspond to oscillations at the band edge, have a single-peak or saddle-like intensity pattern, whereas the higher order modes exhibit more complex patterns of nodes and antinodes. The intensity pattern of the fundamental modes was found to depend on the coupling strength, with peaks in intensity at the ends of the structure for weak coupling and maximum intensity at the center for strong coupling. We have also investigated the hole-filling factor dependence and found that a change in the mode that has lowest threshold gain occurs at a value of 0.3. This analysis provides a deeper understanding of photonic crystal lasers and will allow more effective optimization of their design, such as varying the unit holes to include triangular and elliptical as well as circular shapes, a prospect that we leave to future work.

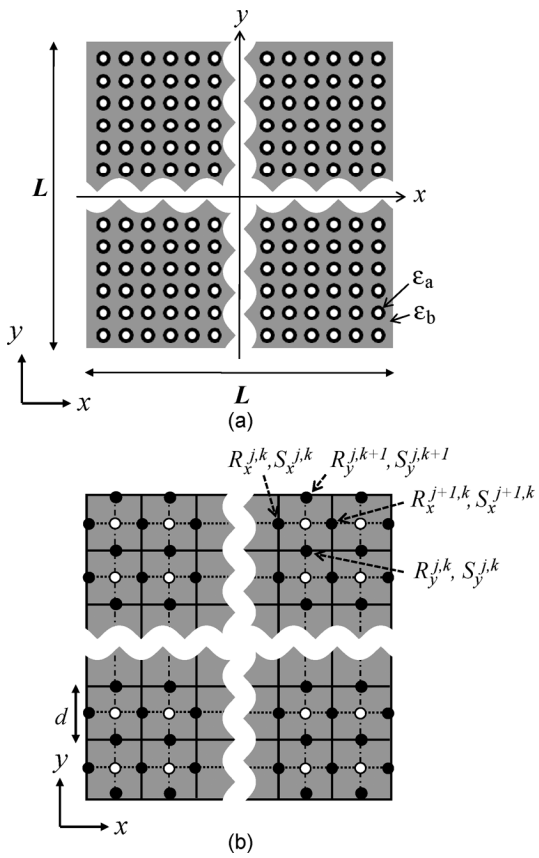

Fig. 10. (a) Schematic illustration of calculation model for the photonic crystal cavity. (b) Segmentation used for the finite difference method. The complex amplitudes are defined at the positions of the black dots, and calculations are carried out at the positions of the white dots.

APPENDIX

A set of coupled wave equations (17) was numerically solved using the finite difference method. Fig. 10(a) illustrates the calculation model, where a square photonic crystal cavity with a side of length L is considered. We note that the typical number of periods in the x and y directions of the actual devices is several hundred, whereas for the calculations we segmented this photonic crystal cavity into a 17 × 17 matrix (for Fig. 8, we used a 9 × 9 matrix), as shown in Fig. 10(b). We define the complex amplitudes R_x, S_x, R_y, S_y at the positions denoted by black dots, and we solve (17) for each white dot using the complex amplitudes of the neighboring black dots. For example, the difference equation corresponding to (17a) is written in the form

$$\begin{aligned}(\alpha-\kappa_0-i\delta)\frac{R_x^{j,k}+R_x^{j+1,k}}{2}-\frac{R_x^{j+1,k}-R_x^{j,k}}{d}\\ =i\frac{4\kappa_1^2}{\beta_0}\frac{R_x^{j,k}+R_x^{j+1,k}}{2}+(i\kappa_3-\kappa_0)\frac{S_x^{j,k}+S_x^{j+1,k}}{2}\\ +i\frac{2\kappa_1^2}{\beta_0}\frac{S_y^{j,k}+S_y^{j,k+1}}{2}+i\frac{2\kappa_1^2}{\beta_0}\frac{R_y^{j,k}+R_y^{j,k+1}}{2}\end{aligned} \quad \text{(A1)}$$

where d is the side length of one segment, and j and k denote the index along the x and y directions, respectively. At all the surrounding boundaries, we set the facet reflection to zero:

$$R_x\left(-\frac{L}{2},y\right)=S_x\left(\frac{L}{2},y\right)=R_y\left(x,-\frac{L}{2}\right)=S_y\left(x,\frac{L}{2}\right)=0. \quad \text{(A2)}$$

By solving the eigenvalue problem for the sets of difference equations, we obtain the eigenvalue $(\alpha - i\delta)$ and the eigenvectors ($R_x^{j,k}, S_x^{j,k}, R_y^{j,k}, S_y^{j,k}$, etc.).

ACKNOWLEDGMENT

The authors are grateful to Dr. M. Okano and Dr. M. Yokoyama for helpful discussion.

REFERENCES

[1] M. Imada, S. Noda, A. Chutinan, T. Tokuda, M. Murata, and G. Sasaki, "Coherent two-dimensional lasing action in surface-emitting laser with triangular-lattice photonic crystal structure," *Appl. Phys. Lett.*, vol. 75, pp. 316–318, 1999.

[2] M. Meier, A. Mekis, A. Dodabalapur, A. Timko, R. E. Slusher, J. D. Joannopoulos, and O. Nalamasu, "Laser action from two-dimensional distributed feedback in photonic crystals," *Appl. Phys. Lett.*, vol. 74, pp. 7–9, 1999.

[3] S. Noda, M. Yokoyama, M. Imada, A. Chutinan, and M. Mochizuki, "Polarization mode control of two-dimensional photonic crystal laser by unit cell structure design," *Science*, vol. 293, pp. 1123–1125, 2001.

[4] M. Imada, A. Chutinan, S. Noda, and M. Mochizuki, "Multidirectionally distributed feedback photonic crystal lasers," *Phys. Rev. B*, vol. 65, p. 195306, 2002.

[5] G. A. Turnbull, P. Andrew, W. L. Barnes, and I. D. W. Samuel, "Operating characteristics of a semiconducting polymer laser pumped by a microchip laser," *Appl. Phys. Lett.*, vol. 82, pp. 313–315, 2003.

[6] I. Vurgaftman and J. R. Meyer, "Design optimization for high-brightness surface-emitting photonic-crystal distributed-feedback lasers," *IEEE J. Quantum Electron.*, vol. 39, no. 6, pp. 689–700, Jun. 2003.

[7] E. Miyai, K. Sakai, T. Okano, W. Kunishi, D. Ohnishi, and S. Noda, "Lasers producing tailored beams," *Nature*, vol. 441, p. 946, 2006.

[8] D. Ohnishi, T. Okano, M. Imada, and S. Noda, "Room temperature continuous wave operation of a surface-emitting two-dimensional photonic crystal diode laser," *Opt. Express*, vol. 12, pp. 1562–1568, 2004.

[9] M. Kim, C. S. Kim, W. W. Bewley, J. R. Lindle, C. L. Canedy, I. Vurgaftman, and J. R. Meyer, "Surface-emitting photonic-crystal distributed-feedback laser for the midinfrared," *Appl. Phys. Lett.*, vol. 88, p. 191105, 2006.

[10] L. Sirigu, R. Terazzi, M. I. Amanti, M. Giovannini, and J. Faist, "Terahertz quantum cascade lasers based on two-dimensional photonic crystal resonators," *Opt. Express*, vol. 16, pp. 5206–5217, 2008.

[11] Y. Chassagneux, R. Colombelli, W. Maineult, S. Barbieri, H. E. Beere, D. A. Ritchie, S. P. Khanna, E. H. Linfield, and A. G. Davies, "Electrically pumped photonic-crystal terahertz lasers controlled by boundary conditions," *Nature*, vol. 457, pp. 174–178, 2009.

[12] H. Matsubara, S. Yoshimoto, H. Saito, Y. Jianglin, Y. Tanaka, and S. Noda, "GaN photonic-crystal surface-emitting laser at blue-violet wavelengths," *Science*, vol. 319, pp. 445–447, 2008.

[13] T. C. Lu, S. W. Chen, L. F. Lin, T. T. Kao, C. C. Kao, P. Yu, H. C. Kuo, and S. C. Wang, "GaN-based two-dimensional surface-emitting photonic crystal lasers with AlN/GaN distributed Bragg reflector," *Appl. Phys. Lett.*, vol. 92, p. 011129, 2008.

[14] M. Yokoyama and S. Noda, "Finite-difference time-domain simulation of two-dimensional photonic crystal surface-emitting laser," *Opt. Express*, vol. 13, pp. 2869–2880, 2005.

[15] K. Sakai, E. Miyai, T. Sakaguchi, D. Ohnishi, T. Okano, and S. Noda, "Lasing band-edge identification for a surface-emitting photonic crystal laser," *IEEE J. Sel. Areas Commun.*, vol. 23, no. 7, pp. 1335–1340, Jul. 2005.

[16] H. Kogelnik and C. V. Shank, "Coupled-wave theory of distributed feedback lasers," *J. Appl. Phys.*, vol. 43, pp. 2327–2335, 1972.

[17] K. Sakai, E. Miyai, and S. Noda, "Two-dimensional coupled wave theory for square-lattice photonic-crystal lasers with TM-polarization," *Opt. Express*, vol. 15, pp. 3981–3990, 2007.

[18] K. Sakai, E. Miyai, and S. Noda, "Coupled-wave model for square-lattice two-dimensional photonic crystal with transverse-electric-like mode," *Appl. Phys. Lett.*, vol. 89, p. 021101, 2006.
[19] M. Plihal and A. A. Maradudin, "Photonic band structure of two-dimensional systems: The triangular lattice," *Phys. Rev. B*, vol. 44, pp. 8565–8571, 1991.
[20] H. Kogelnik, "Coupled wave theory for thick hologram gratings," *Bell Syst. Tech. J.*, vol. 48, pp. 2909–2947, 1969.
[21] K. Sakai, J. Yue, and S. Noda, "Coupled-wave model for triangular-lattice photonic crystal with transverse electric polarization," *Opt. Express*, vol. 16, pp. 6033–6040, 2008.
[22] R. F. Kazarinov and C. H. Henry, "Second-order distributed feedback lasers with mode selection provided by first-order radiation losses," *IEEE J. Quantum Electron.*, vol. 21, no. 2, pp. 144–150, Feb. 1985.
[23] Y. Kurosaka, K. Sakai, E. Miyai, and S. Noda, "Controlling vertical optical confinement in two-dimensional surface-emitting photonic-crystal lasers by shape of air holes," *Opt. Express*, vol. 16, pp. 18485–18494, 2008.

Kyosuke Sakai (S'04–M'07) was born in Hokkaido, Japan, in 1977. He received the B.S. degree in physics, the M.S. degrees in electronics, and the Ph.D. degree from Kyoto University, Kyoto, Japan, in 2002, 2004, and 2007, respectively.

He is currently an Assistant Professor of Kyoto University Pioneering Research Unit for Next Generation, Kyoto, Japan. His research interest covers physics and photonics including photonic crystal, lasers, vector beams, optical angular momentum, optical tweezers, and bio-photonics.

Dr. Sakai is a member of the Optical Society of America and the Japan Society of Applied Physics.

Eiji Miyai was born in Kagawa, Japan, in 1967. He received the B.S. degree from Shizuoka University, Shizuoka, Japan, in 1991, the M.S. from Kochi University, Kochi, Japan, in 1996, and the Ph.D. degree from Hokkaido University, Sapporo, Japan, in 1999, all in physics.

From 1999 to 2001, he worked as a Postdoctoral Researcher at the Research Institute for Electronic Science, Hokkaido University, where he was engaged in research on photonic crystal cavities. In 2001, he joined Kyoto University, Kyoto, Japan, as a Postdoctoral Researcher of the Department of Electronic Science and Engineering. In 2007, he joined ROHM Company, Ltd., Kyoto, Japan, where he is currently a Research Engineer. His research interest is theoretical analysis of optical devices based on photonic crystals.

Dr. Miyai is a member of the Japan Society of Applied Physics (JSAP) and the Physical Society of Japan (JPS).

Susumu Noda (M'92–SM'06–F'08) received the B.S., M.S., and Ph.D. degrees from Kyoto University, Kyoto, Japan, in 1982, 1984, and 1991, respectively, all in electronics. He received an honorary degree from Gent University, Gent, Belgium, In 2006.

From 1984 to 1988, he was with the Mitsubishi Electric Corporation, and he joined Kyoto University in 1988. Currently, he is a Professor with the Department of Electronic Science and Engineering and a Director of Photonics and Electronics Science and Engineering Center (PESEC), Kyoto University. His research interest covers physics and applications of photonic and quantum nanostructures, including photonic crystals and quantum dots.

Prof. Noda received various awards, including the IBM Science Award in 2000, the Japan Society of Applied Physics Achievement Award on Quantum Electronics in 2005, and the OSA Joseph Fraunhofer Award/Robert M. Burley Prize in 2006, and the IEEE Nanotechnology Pioneering Award. From 2003 to 2005, he served as IEEE/LEOS Distinguished Lecturer.